Supporting Information

Photoelectron "Bridge" is Introduced to Realize the Precise Transport of C_3N_5-CoPc Interface Charge for Efficient Photocatalytic H_2O_2 Production

Ruixin Chen[1], Wei Gan[1], Jun Guo[2], Yuqing Lu[1], Sheng Ding[1], Run Liu[1], Shouguo Wang[1], Miao Zhang[1]*, Qingqing Yang[1]*, Zhaoqi Sun[1]*

1. School of Materials Science and Engineering, Anhui University, Hefei, Anhui 230601, PR China.

2. School of Electronic Engineering, Huainan Normal University, Huainan, 232038, PR China.

*Corresponding author: zhmiao@ahu.edu.cn; qqyang@ahu.edu.cn; szq@ahu.edu.cn.

Text S1. Materials characterizations

The morphology of the samples was studied by field-emission scanning electron microscope (FE-SEM, Hitachi regulus 8230) and transmission electron microscope (TEM, JEM-2100) with an accelerating voltage of 200 kV. X-ray diffractometer (XRD, MAC, M18XHF) with copper Kα radiation (λ = 1.5406 Å) as the radiation source were used to examined the crystal structure and phases of materials. The N_2 adsorption/desorption curve was determined by BET measurements using a Micromeritics ASAP2460 surface area analyzer. The X-ray photoelectron spectroscopy (XPS) measurements were performed with ESCALAB-250 spectrometer to analyze the elemental composition of the sample surface. The UV-vis diffuse reflectance spectra were performed by a Shimadzu UV-2550 spectrometer. The photoluminescence (PL) emission spectra were measured on a luminescence spectrophotometer (Hitachi FL-7000) (370 nm excitation). Fourier transform-infrared spectrometer (FT-IR) measurements were performed on a Vertex80 + hyperion 2000. Atomic Force Microscope (AFM) images were measured on Hitachi AFM 5500 M. The electron paramagnetic resonance (EPR) spectra were recorded on a Bruker EMX Plus spectrometer.

Text S2. Photoelectrochemical Measurements

The transient photocurrent response, Electrochemical impedance spectroscopy (EIS), and Mott-Schottky plot were tested on three-electrode CHI660E electrochemical workstation with the photocatalysts as the working electrodes, saturated calomel electrode as reference electrode, and platinum foil electrode as counter electrode in 0.5 M Na_2SO_4 solution. The working electrodes were prepared by dropping the sample suspension containing 10 mg powder and 200 μL ethanol onto the cleaned FTO conductive glass (1×1 cm^2). And a 300 W xenon lamp was used as the irradiation source.

Text S3. DFT Calculations

The periodic model was used to simulate the ORR reaction happened on C_3N_5-P-CoPc. The adsorption energy (E_{ads}) of O_2 was calculated as follows:

$$E_{ads}(O_2) = E(*O_2) - E(*) - E(O_2) \quad (4)$$

Where $E(*O_2)$, $E(*)$, and $E(O_2)$ are the total energy of samples with O_2 adsorbates on the surface, the energy of pristine samples surface and O_2, respectively.

The change in Gibbs free energy (ΔG) at each step of the reduction process is calculated by correcting the zero-point energy and entropy of the DFT. And the calculation formula follows equation:

$$\Delta G = \Delta E + \Delta ZPE - T\Delta S + \Delta G_U \quad (5)$$

Where the ΔE is obtained from DFT calculations, ΔZPE is zero-point energy, T is 298.1 K and ΔS is entropy change. ΔG_U = - eU is the free energy contribution caused by electrode potential U.

In addition, we provide the list of the reaction equation used of for calculation of each step, the equation is as follows:

$$O_2 + * \rightarrow *O_2 \quad (6)$$

$$*O_2 + H^+ + e^- \rightarrow *OOH \quad (7)$$

$$*OOH + H^+ + e^- \rightarrow *H_2O_2 \quad (8)$$

$$*H_2O_2 \rightarrow * + H_2O_2 \quad (9)$$

Where * represents the surface-active structure.

Text S4. Apparent quantum yield (AQY) calculation

A 300 W Xe lamp with different bandpass filters of 400, 420, 450, and 500 nm was used to test the AQY of the H_2O_2 photocatalytic production process. The light intensity was adjusted to be 100 $W \cdot m^{-2}$, and the irradiated area was 19.625 cm^2. After irradiation 1 h, the generated H_2O_2 concentration was measured. And the AQY value was calculated by the following formula:

$$\mathrm{AQY}(\%) = 2 \times \frac{N_{H_2O_2} \cdot N_A \cdot h \cdot c}{I \cdot S \cdot t \cdot \lambda} \times 100\% \quad (1)$$

Where is N_{H2O2} the measured amount of the H_2O_2 (mol), NA is the Avogadro constant

(6.02×10^{23} mol^{-1}), h represents the Planck constant (6.62×10^{-34} J·s), c is the speed of light (3×10^{8} $m \cdot s^{-1}$), S is the irradiation area (19.625 cm^2), I represents the irradiation intensity (100 $W \cdot m^{-2}$), t is the irradiation time (s), and λ represents the wavelength of incident light (m). The corresponding test data are listed in Table S1.

Table S1. Wavelength-dependent AQY for C_3N_5-8P-0.9CoPc in potocatalytic H_2O_2 generation.

Wavelength (nm)	Irradiation intensity (W m^{-2})	Irradiation area (cm^2)	Irradiation time (s)	H_2O_2 yield/μmol	AQY/%
400 nm	13.1	19.63	3600	37.00	23.89%
420 nm	14.2	19.63	3600	37.05	21.02%
450 nm	16.2	19.63	3600	34.00	15.78%
500 nm	17.1	19.63	3600	31.50	12.47%

Text S5. Rotating ring-disk electrode (RRDE) measurements

RRDE measurements were performed through an electrochemical workstation (Chenhua CHI 760E). The counter electrode, the reference electrode and working electrode were Pt wire, Ag/AgCl electrode and glassy carbon electrode coated with catalysts, respectively. The linear sweep voltammetry (LSV) curves were acquired in an O_2-saturated 0.1 M phosphate buffer solution, the scan rate was 10 $mV \cdot s^{-1}$, and the speed of the working electrode was set at 1600 rpm.

The number of transferred electrons in ORR is calculated as follow:

$$n = 4I_d\left(I_d + \frac{I_r}{N}\right) \quad (2)$$

and the selectivity of H_2O_2 is calculated by the following formula:

$$H_2O_2(\%) = 200 \times (I_r/N)/(I_d + I_r/\mathrm{N}) \quad (3)$$

where I_d is the disk current, I_r is the ring current, N represents the collection efficiency (N=0.37).

Text S6. Ultrafast transient absorption (TA) spectroscopy

Femtosecond-TA measurements were conducted by using the Helios (Ultrafast

Systems) pump-probe system in collaboration with a regenerative amplified laser system (Spectra physics). The Ti: sapphire amplifier (Solstice Ace) generated an 800 nm pulse with a repetition rate of 1 kHz, a duration of 120 fs and an energy of 7 mJ/pulse. The output of the amplifier was divided into two parts using a beam splitter, one beam was used to generate the pump pulse with an APOLLO-T (Ultrafast Systems) optical parametric amplifier and the other beam was focused onto sapphire crystal, generating white light supercontinuum (from 420 to 760 nm) for the probe beam. The wavelength and the energy density of pump pulse were 325 nm and 5.0 $\mu J/cm^2$, respectively.

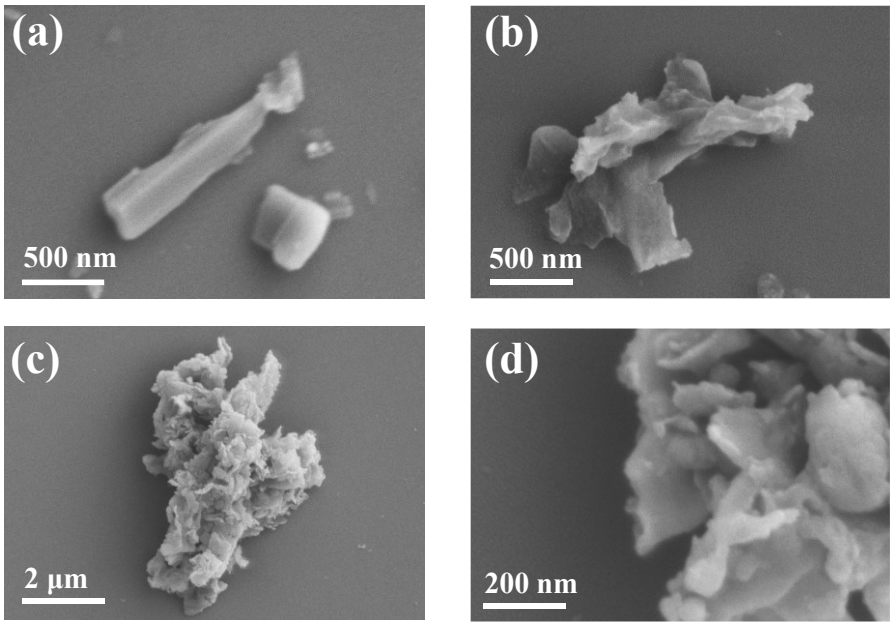

Figure S1. SEM patterns of (a) CoPc, (b) C_3N_5, (c-d) C_3N_5-8P-0.9CoPc.

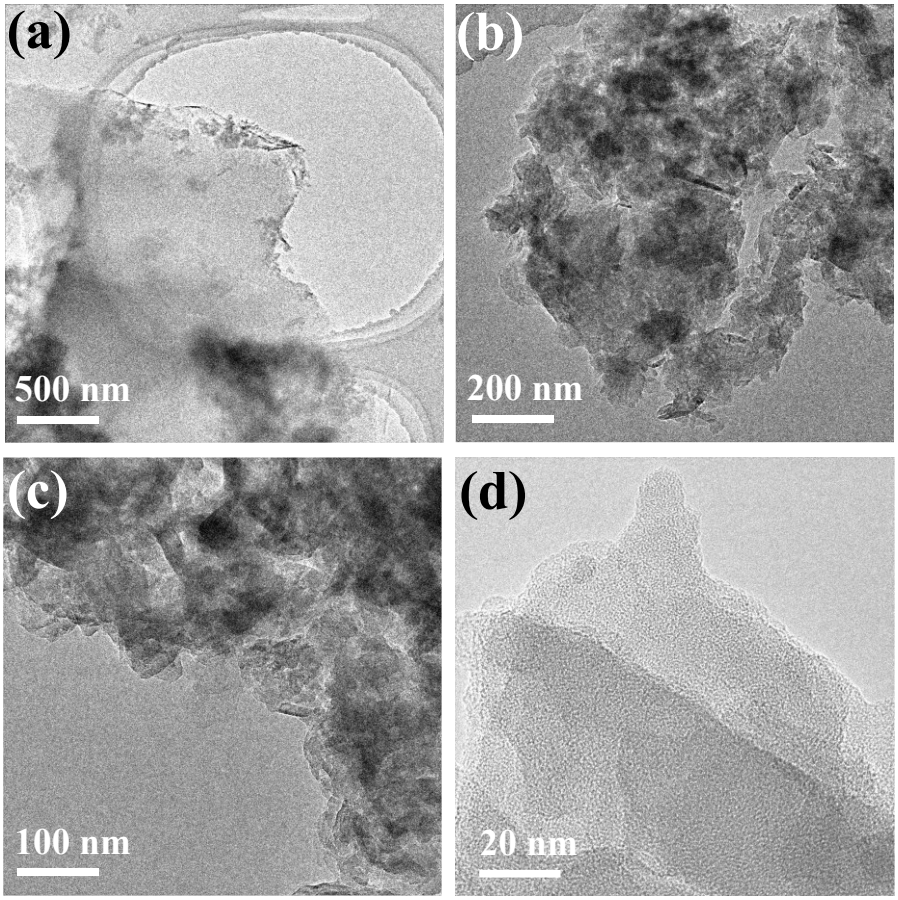

92 **Figure S2.** TEM patterns of C_3N_5-8P-0.9CoPc.

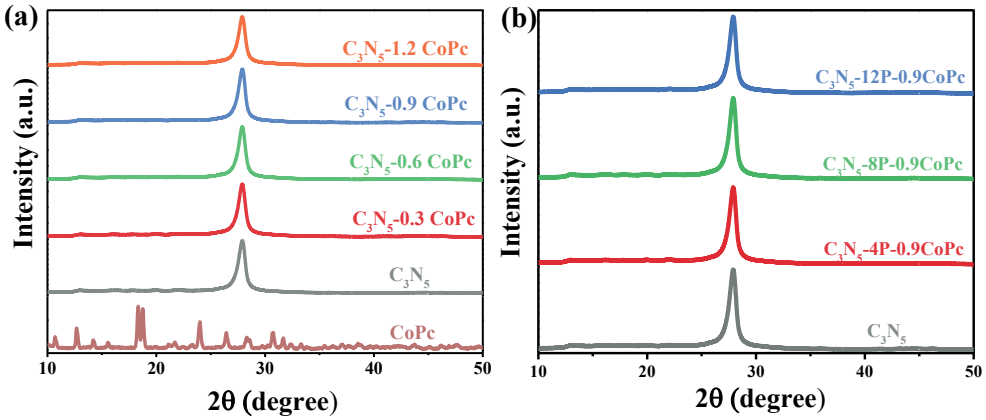

93 **Figure S3.** XRD patterns of (a) C_3N_5 and C_3N_5-XCoPc and (b) C_3N_5-YP-0.9CoPc.

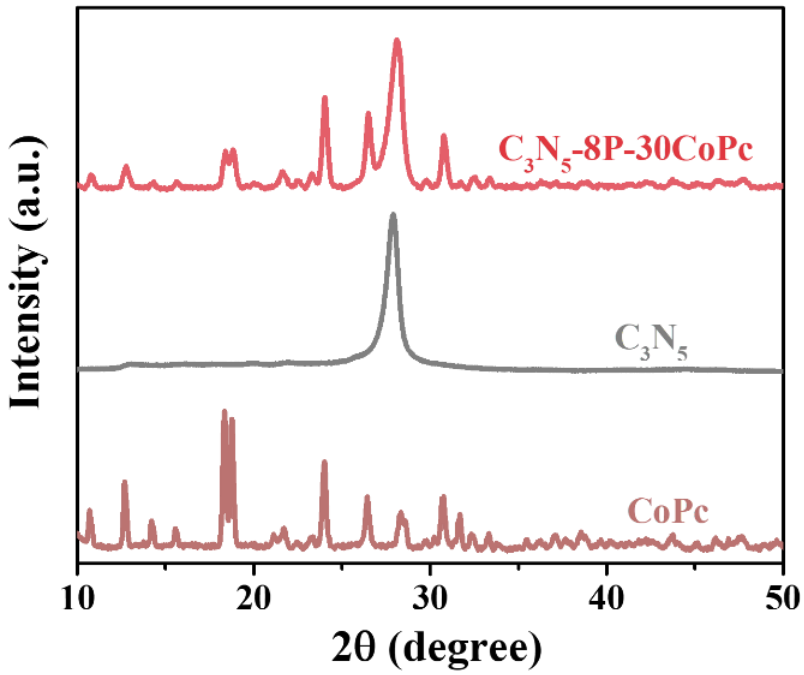

Figure S4. XRD patterns of CoPc, C_3N_5, and C_3N_5-8P-30CoPc.

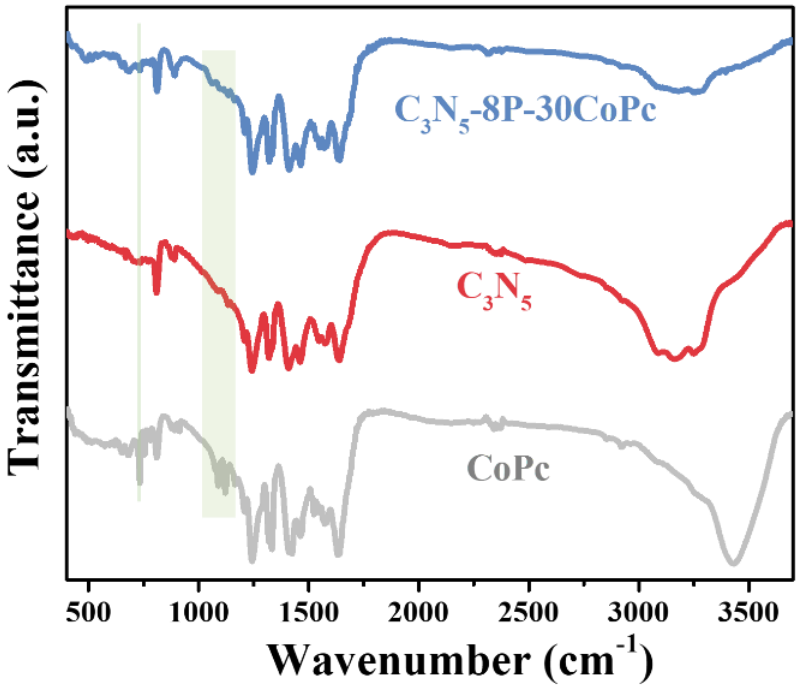

96 **Figure S5.** FTIR patterns of CoPc, C_3N_5, and C_3N_5-8P-30CoPc.

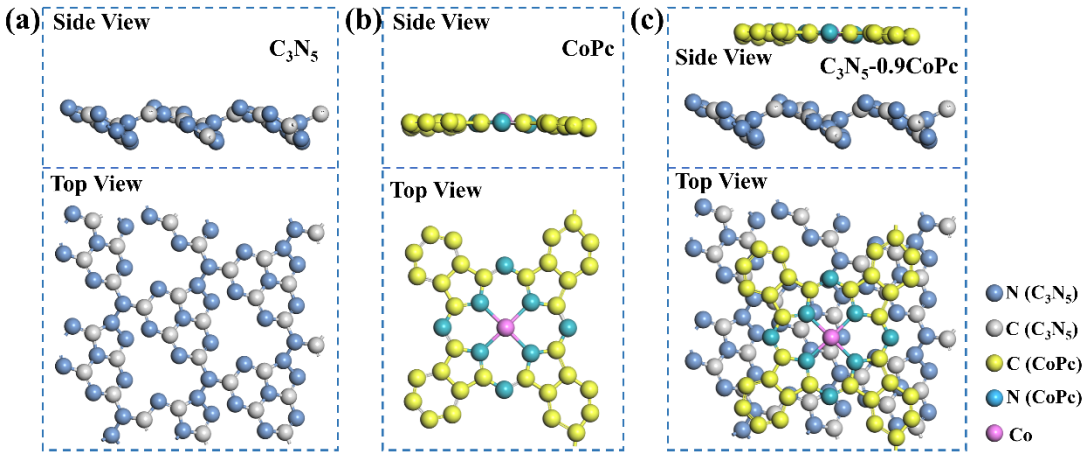

97 **Figure S6.** The model of (a) C_3N_5, (b) CoPc, and (c) C_3N_5-CoPc with side and top view.

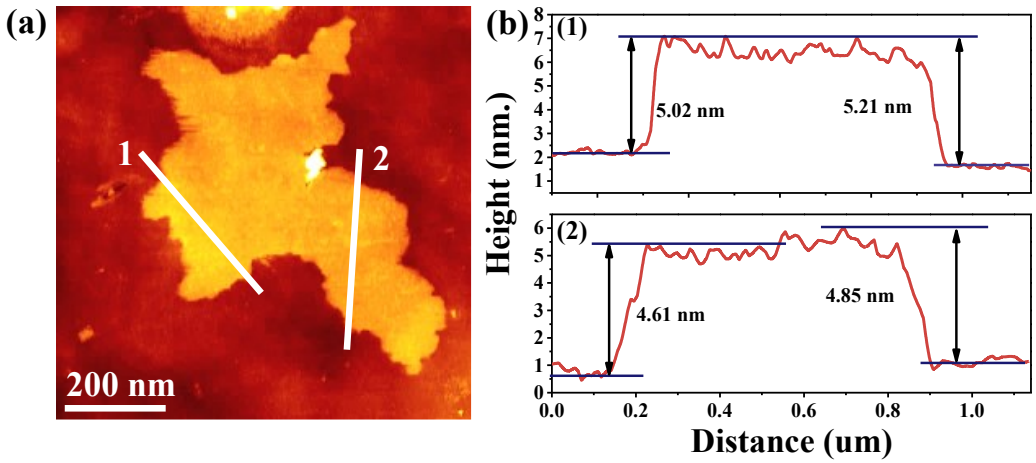

98 **Figure S7.** The (a) AFM image and (b) corresponding height image of C_3N_5.

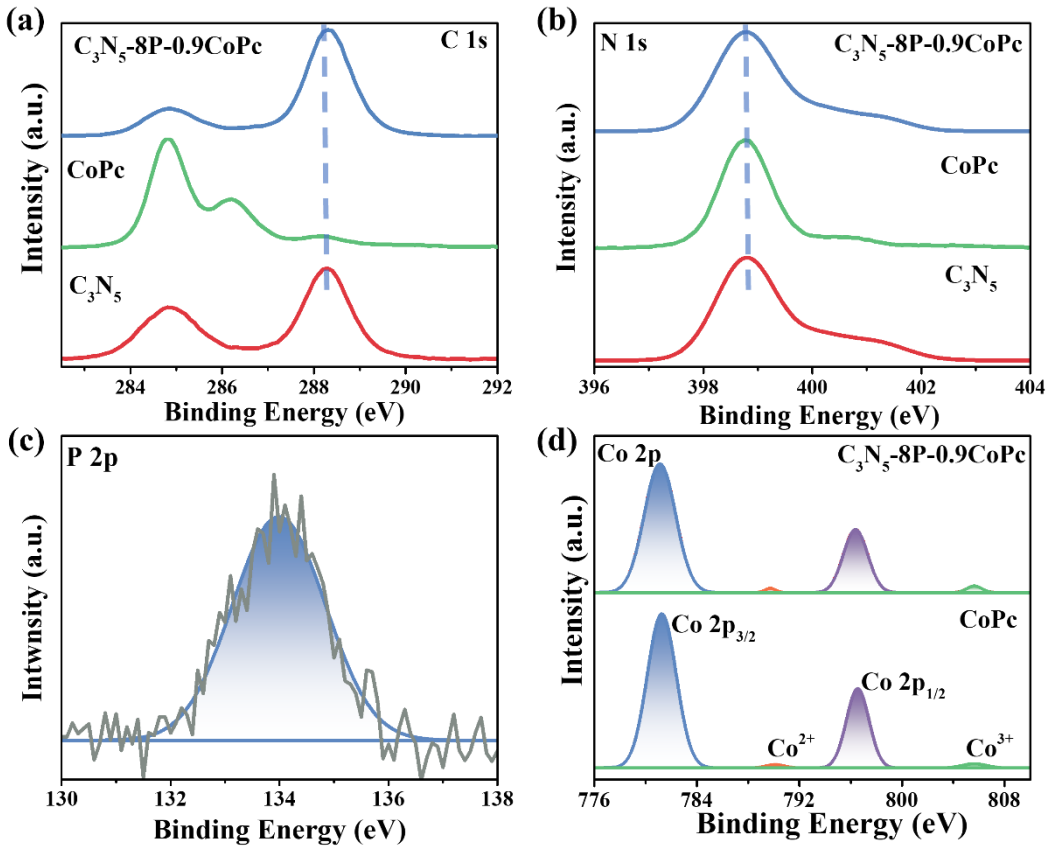

Figure S8. The high-resolution XPS spectra of the C 1s region and (b) the N 1s region for C_3N_5, CoPc, and C_3N_5-8P-0.9CoPc, respectively. (c) The high-resolution XPS spectra of P 2p region for C_3N_5-8P-0.9CoPc. (d) The high resolution XPS spectra of the Co 2p region for CoPc and C_3N_5-8P-0.9CoPc, respectively.

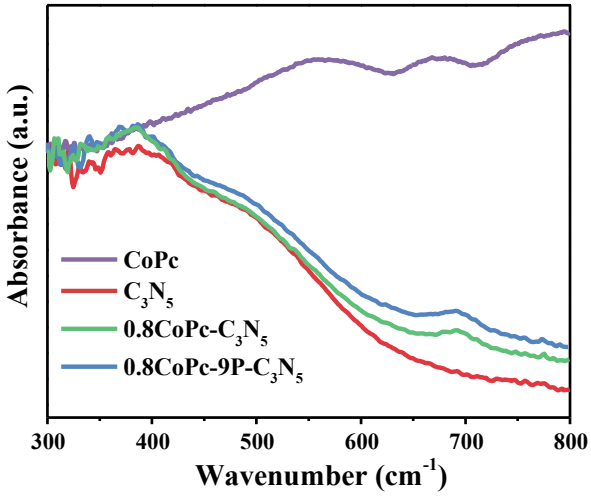

103 **Figure S9.** UV-vis absorption spectra of the photocatalytic.

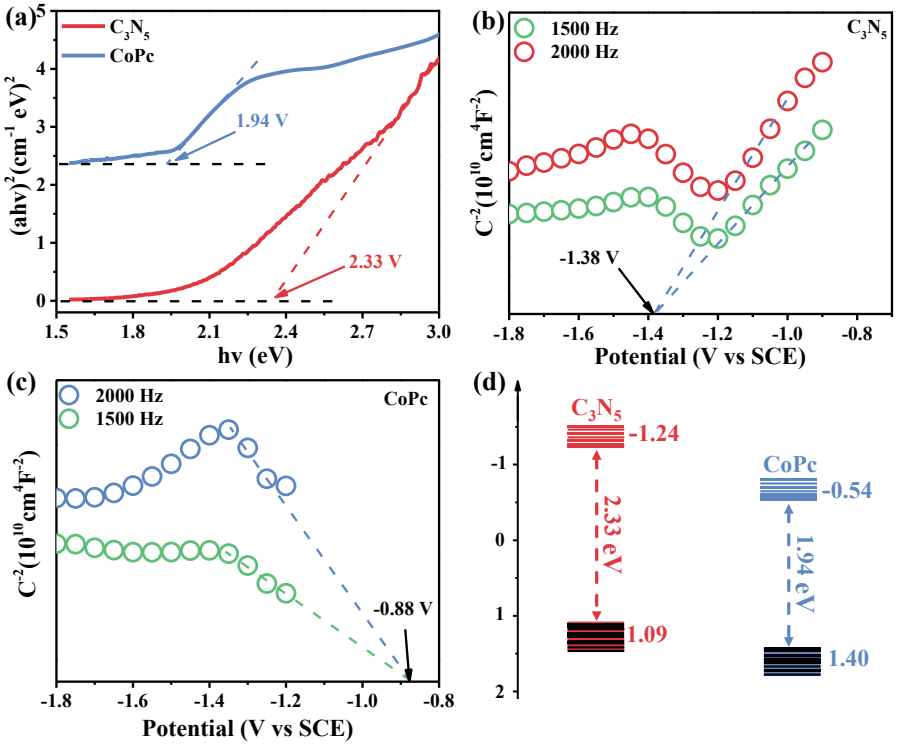

Figure S10. (a) Absorption edges of C_3N_5 and CoPc; Mott-Schottky plots of (b) C_3N_5, (c) CoPc; (d) band structure diagram of C_3N_5 and CoPc.

Note: The band gaps of C_3N_5 and CoPc are estimated using the Tauc formula, as shown in Figure S10a. The calculated band gap values of C_3N_5 and CoPc are 2.33 and 1.94 eV, respectively. The flat band potential (E_{fb}) of the samples was measured using Mott-Schottky, and the results are shown in Figure S10b-c. Where the curves of C_3N_5 and CoPc show positive and negative slopes, respectively, indicating that they are n-type, p-type semiconductors, respectively. The E_{fb} of C_3N_5 and CoPc were measured to be -1.38, -0.88 eV (vs. SCE), respectively, which correspond to -1.14 and -0.64 eV versus NHE, respectively ($E_{NHE}=E_{SCE}+0.24$ eV). Generally, the bottom of the conduction band (CB) in n-type semiconductors is 0.1 eV lower than E_{fb}, and the bottom of the valence band (VB) in p-type semiconductors is 0.1 eV higher than E_{fb}. According to the equation of $Eg=E_{VB}-E_{CB}$, the valence band potential (E_{VB}) of C_3N_5 and CoPc were calculated to be 1.09 and 1.40 eV, respectively. The detailed energy band structure of C_3N_5 and CoPc is shown in Figure S10d.

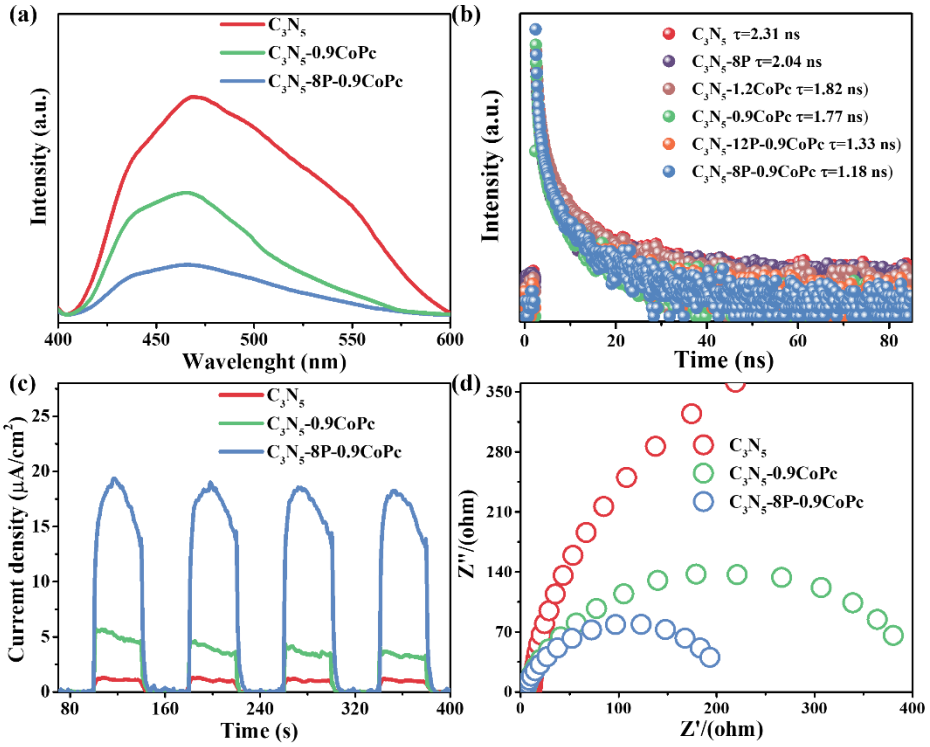

Figure S11. (a) PL spectra, (b) TRPL spectra, (c) photocurrent responses, (d) EIS Nyquist plots of samples.

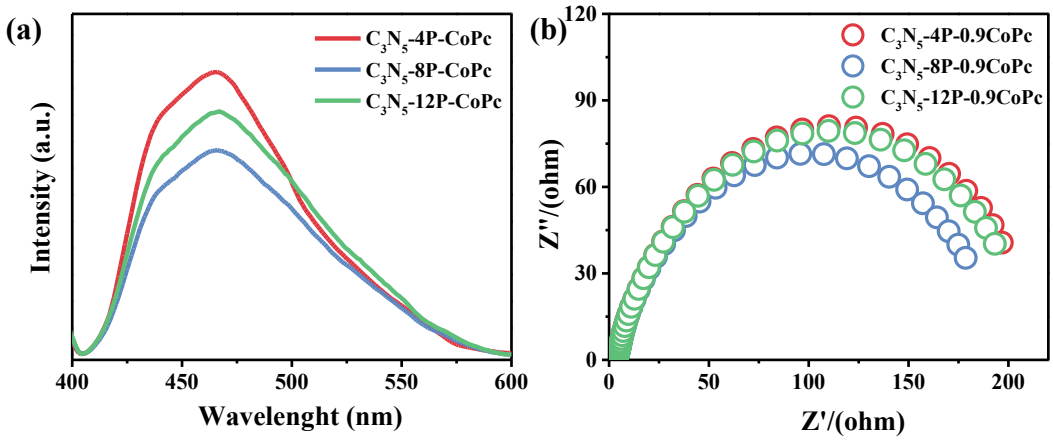

Figure S12. (a) PL spectra, (b) EIS Nyquist plots of C_3N_5-4P-0.9CoPc, C_3N_5-8P-0.9CoPc, and C_3N_5-12P-0.9CoPc.

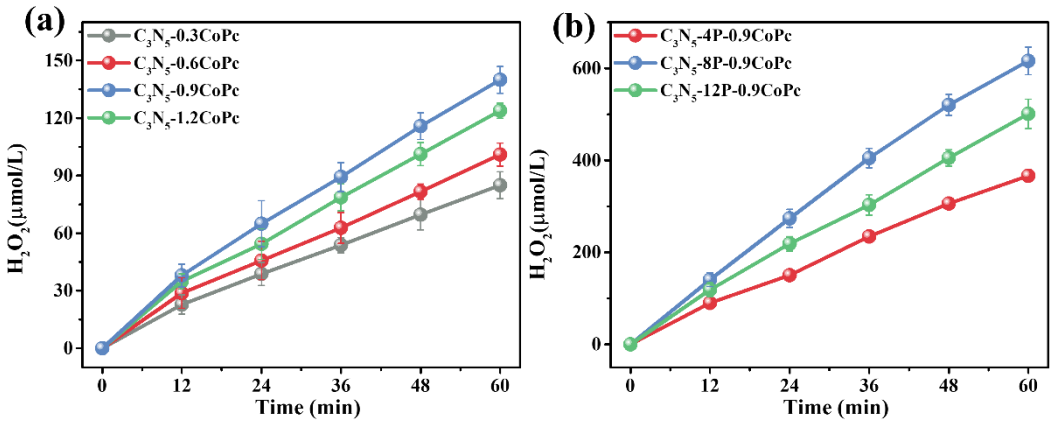

Figure S13. Photocatalytic H_2O_2 production concentration with (a) C_3N_5-XCoPc, (b) C_3N_5-YP-0.9CoPc.

Note: The effects of different mass ratios of CoPc and phosphate to C_3N_5 on the photocatalytic production of H_2O_2 were evaluated, and the results showed that the photocatalytic H_2O_2 production performance of C_3N_5-0.9CoPc was higher when the mass ratio of CoPc to C_3N_5 was 0.9%. When the mass ratio of phosphate to C_3N_5 was 0.8 %, the H_2O_2 yield of the photocatalyst C_3N_5-8P-0.9CoPc reached the highest value (3080.3 μmol g^{-1} h^{-1}). Therefore, the discussion in this paper mainly focuses on the photocatalysts C_3N_5-0.9CoPc and C_3N_5-8P-0.9CoPc.

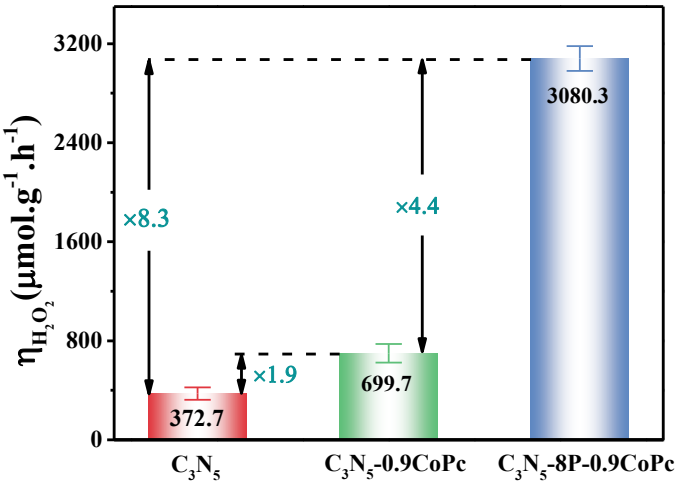

128 **Figure S14.** Photocatalytic H_2O_2 yield of C_3N_5, C_3N_5-0.9CoPc, and C_3N_5-8P-0.9CoPc.

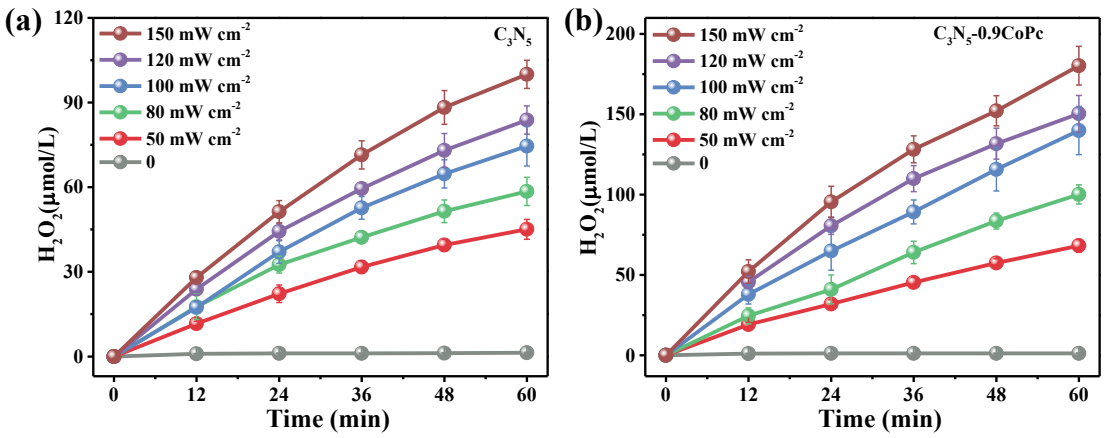

Figure S15. Time course of H_2O_2 production under different light intensity of (a) C_3N_5, (b) C_3N_5-0.9CoPc.

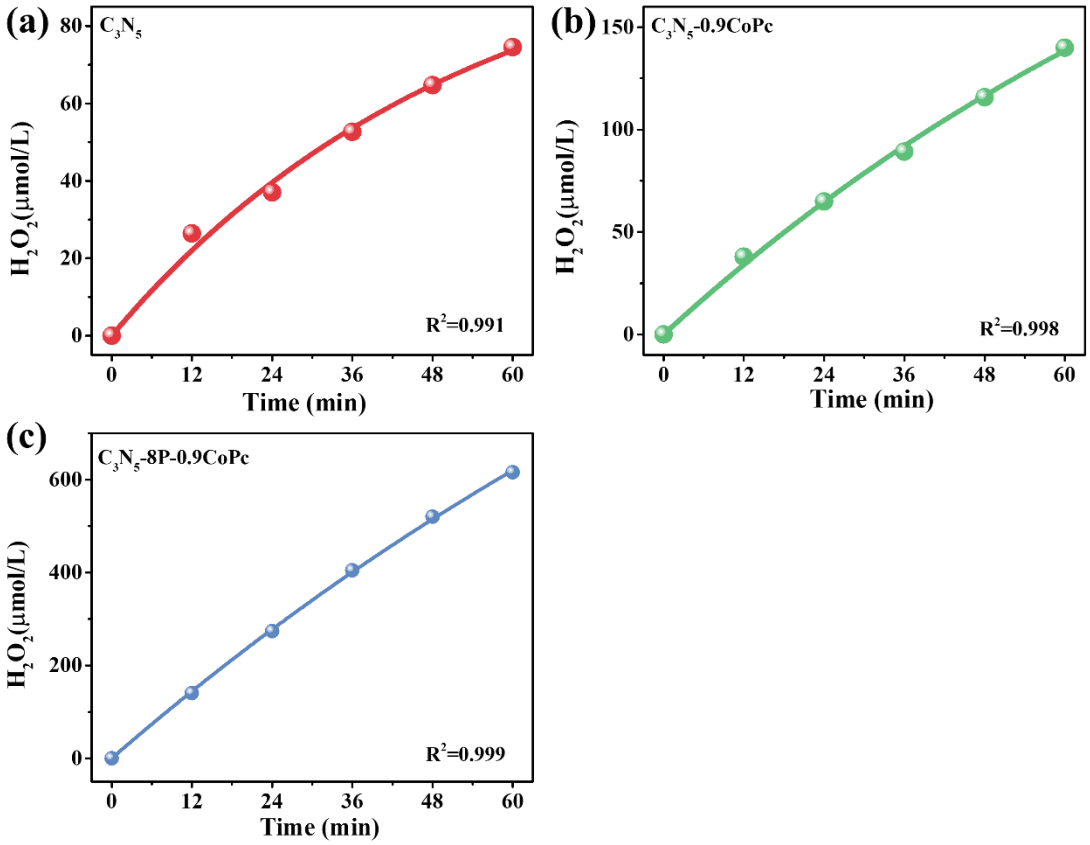

131 **Figure S16.** The fitting concentration-time curves of (a) C_3N_5, (b) C_3N_5-0.9CoPc, (c) C_3N_5-8P-
132 0.9CoPc.

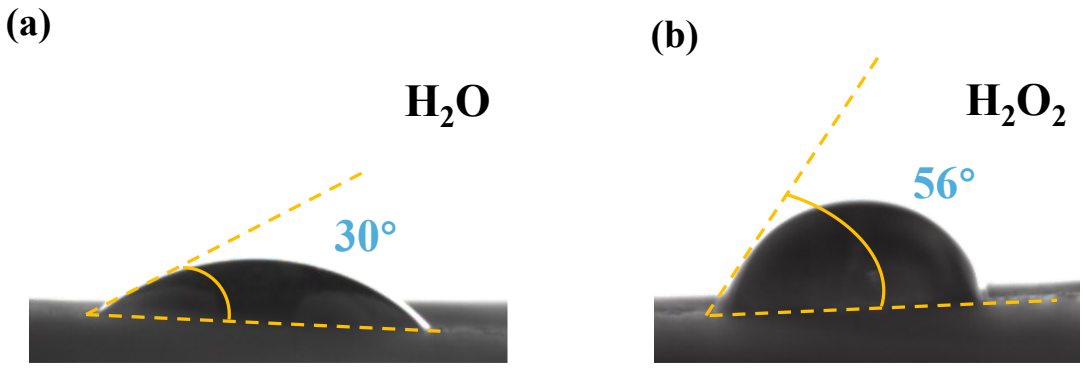

Figure S17. (a) The water contact angle and (b) H_2O_2 contact of C_3N_5-8P-0.9CoPc.

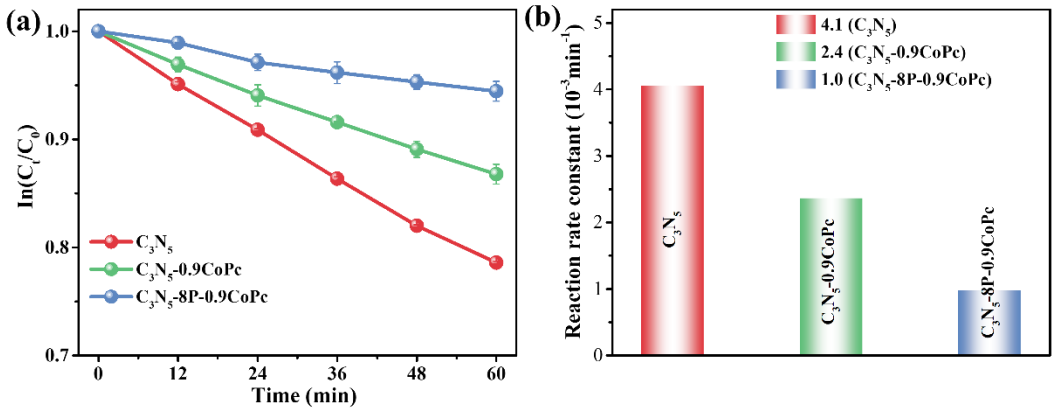

134 **Figure S18.** The (a) photocatalytic decomposition on H_2O_2 of C_3N_5, C_3N_5-0.9CoPc, C_3N_5-8P-0.9CoPc
135 and (b) the corresponding reaction rate constants.

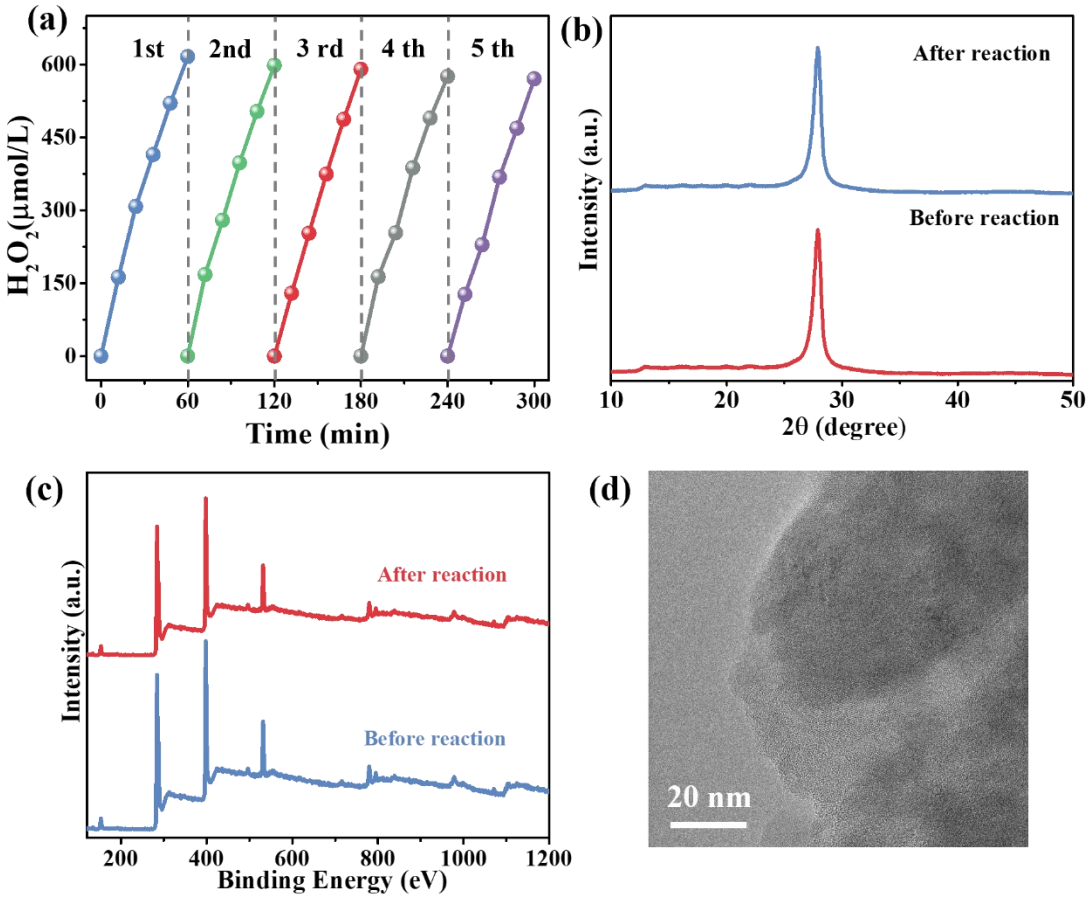

136 **Figure S19.** Cycle experiments of C_3N_5-8P-0.9CoPc; (b) XRD pattern and (c) XPS survey spectra of
137 C_3N_5-8P-0.9CoPc before and after the photocatalytic H_2O_2; (d) TEM image of C_3N_5-8P-0.9CoPc after
138 the photocatalytic H_2O_2.

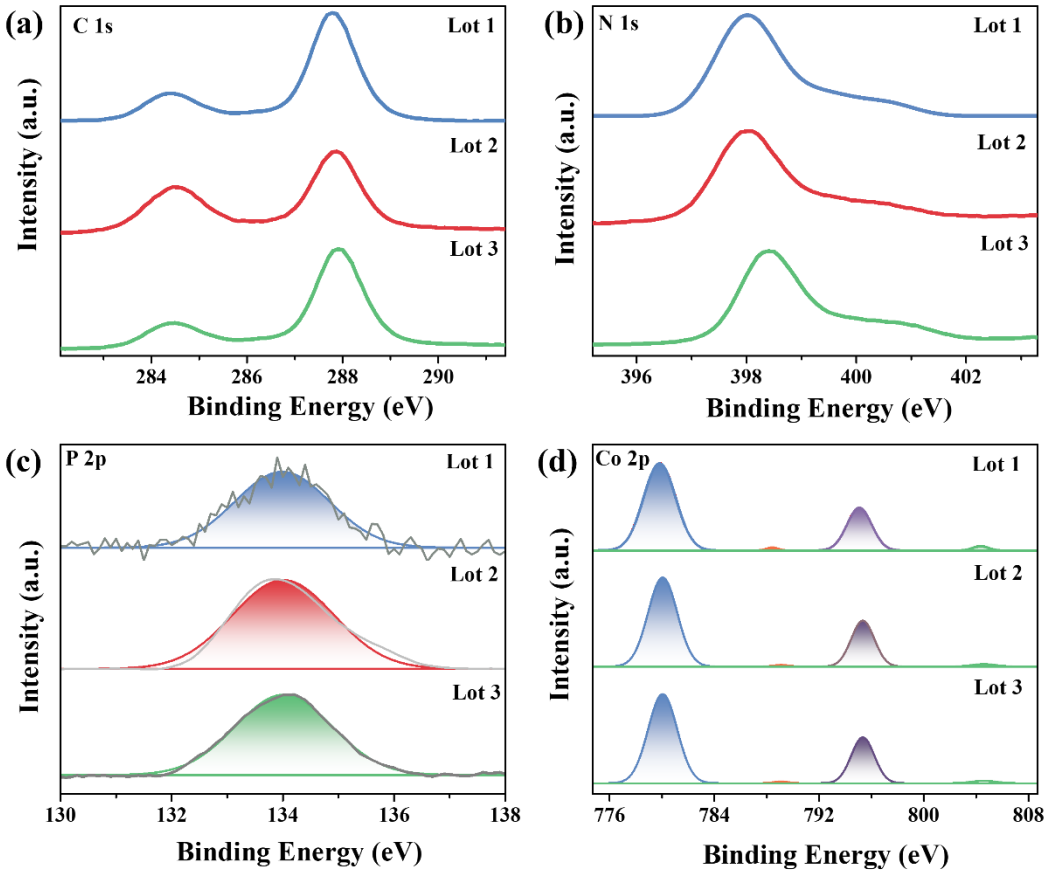

Figure S20. (b) The high-resolution XPS spectra of the C 1s, (b) the N 1s, (c) the P 2p, (d) the Co 2p of different batches of C_3N_5-8P-0.9CoPc.

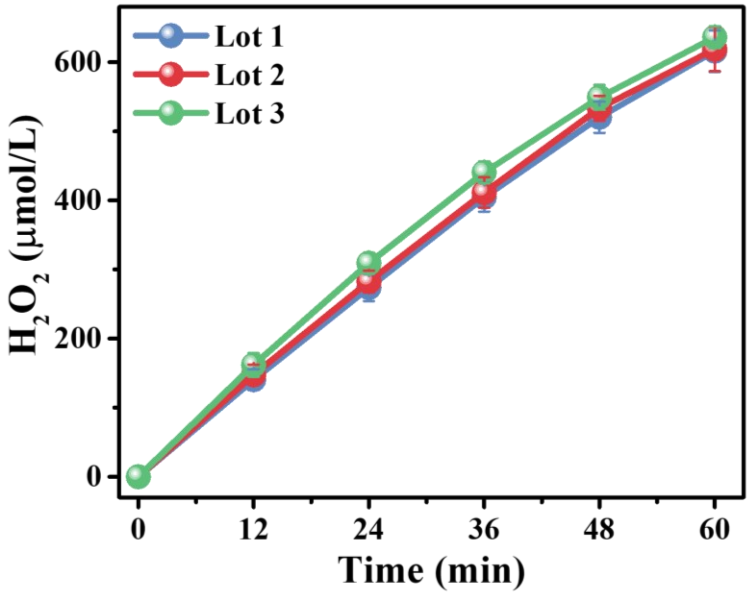

141 **Figure S21.** Photocatalytic H_2O_2 production performance of different batches of C_3N_5-8P-0.9CoPc.

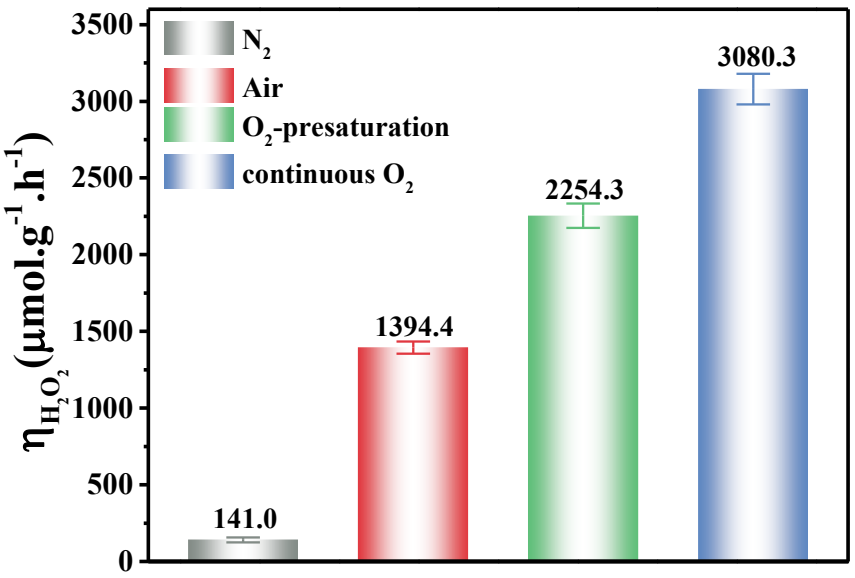

142 **Figure S22.** Photocatalytic H_2O_2 yield of C_3N_5-8P-0.9CoPc under different reaction gases.

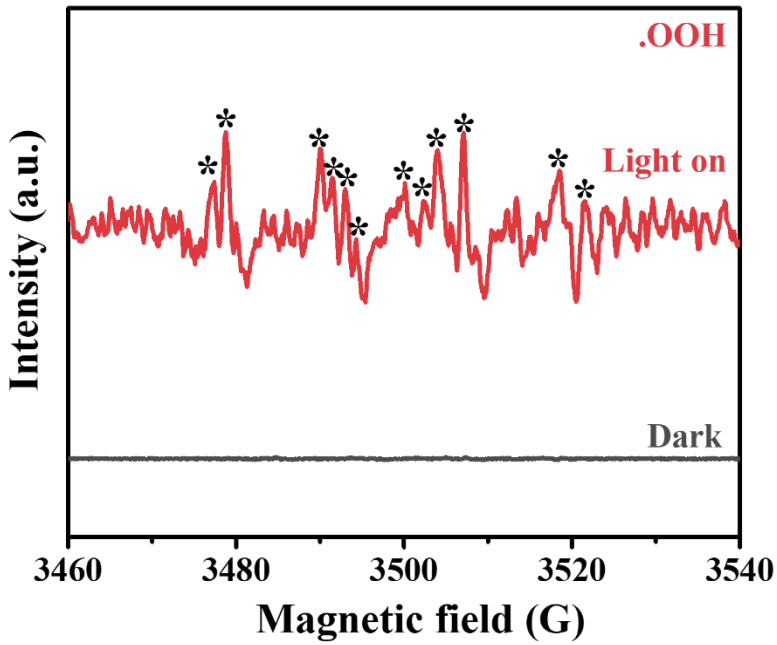

Figure S23. EPR signals of ·OOH for C_3N_5-8P-0.9CoPc under dark and illumination.

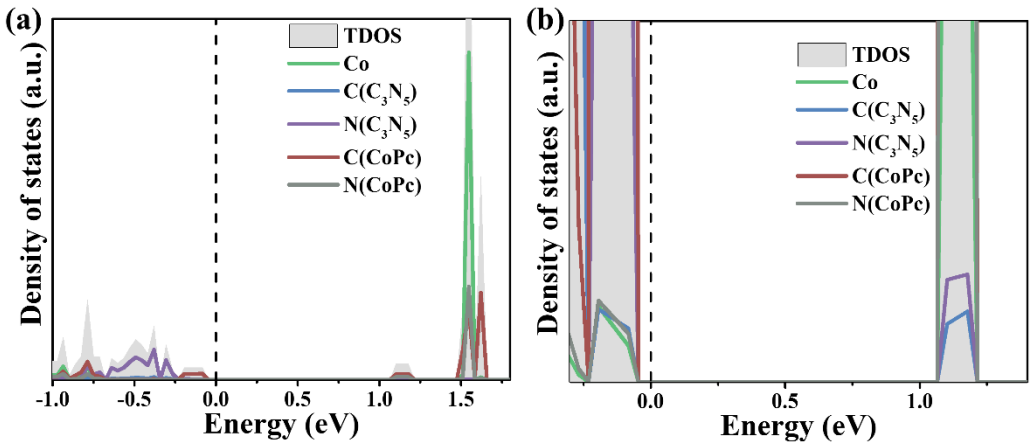

144 **Figure S24.** (a) The PDOS of C_3N_5-0.9CoPc, (b) the enlarged part PDOS of C_3N_5-0.9CoPc.

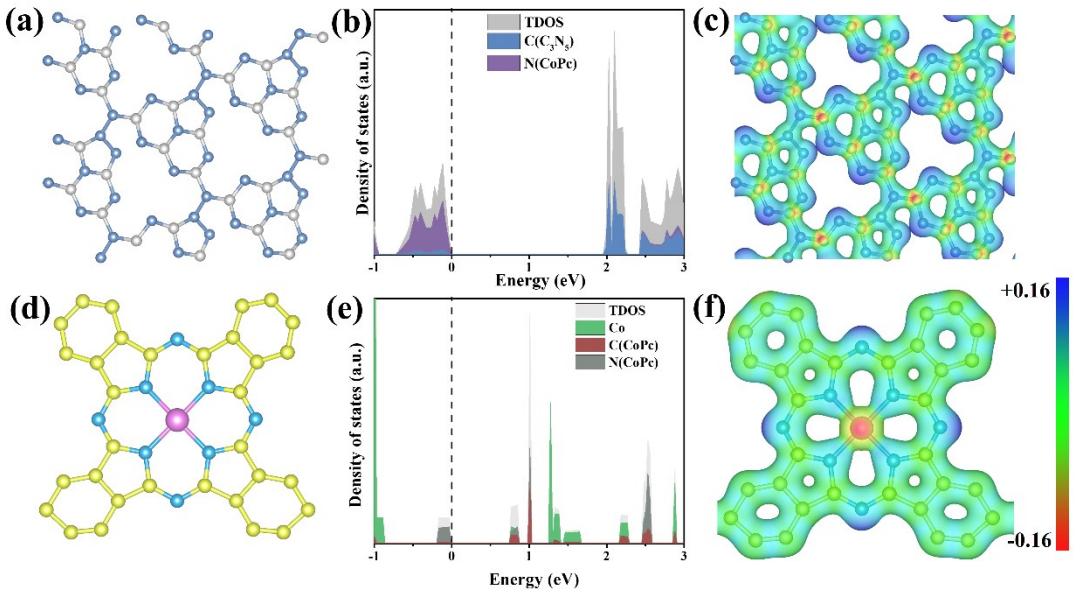

145 **Figure S25.** The optimized structures of (a) C_3N_5, (d) CoPc; the partial density of states (PDOS) of (b)
146 C_3N_5, (e) CoPc; the electrostatic potential spectra of (c) C_3N_5, (f) CoPc.

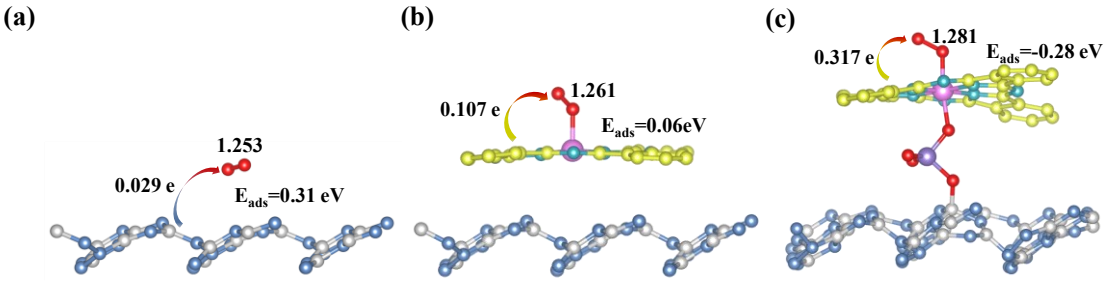

147 **Figure S26.** The optimized adsorption configurations of O_2 on (a) C_3N_5, (b) C_3N_5-0.9CoPc, (c) C_3N_5-
148 8P-0.9CoPc.

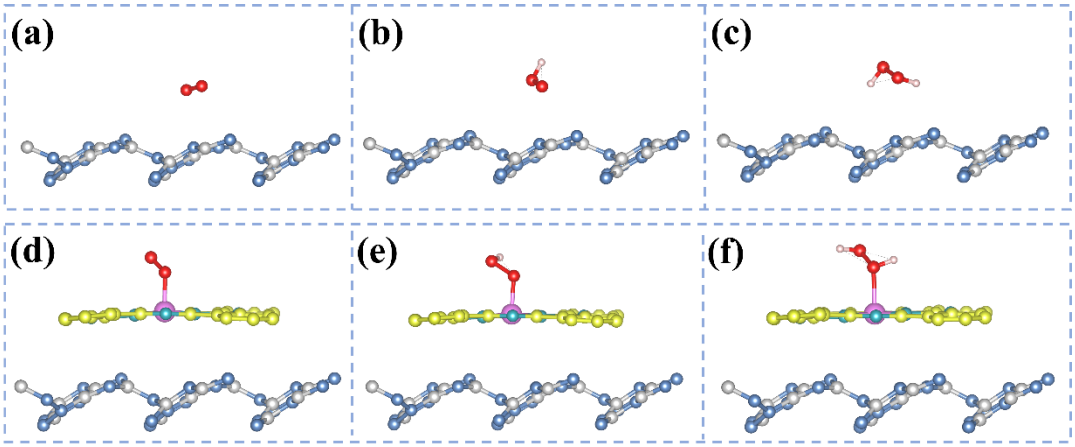

Figure S27. The optimized adsorption configurations of (a) O_2, (b) OOH, (c) HOOH on C_3N_5; the optimized adsorption configurations of (a) O_2, (b) OOH, (c) HOOH on C_3N_5 on C_3N_5-0.9CoPc.

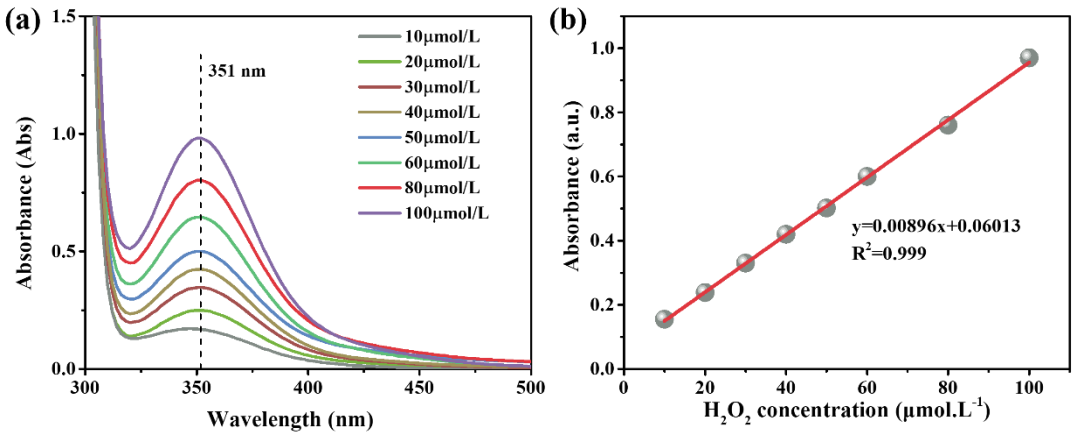

151 **Figure S28.** (a) The UV-vis spectrum changes of H_2O_2 concentration, (b) the linear fitting formula of
152 standard H_2O_2 concentration.

Table S2. Comparison of the H_2O_2 production rate of C_3N_5-8P-0.9CoPc with reported catalysts

Catalysts	Electron donor	Light source	H_2O_2 yield (μmol g^{-1} h^{-1})	AQY 420 nm	Cycle/ efficiency	Ref
CdS-O,Sv	10% IPA	300 W	1620.00	17.60	5/87.2%	[1]
$Ag/ZnFe_2O_4/Ag/Ag_3PO_4$	10% MeOH	300 W	103.00	14.53	5/92.1%	[2]
DCN-15A	20% IPA	300 W	96.80	10.70	3/97.5%	[3]
CKCN-0.03	20% EtOH	300 W	152.60	11.86	-/-	[4]
C_3N_4/AQ	10% IPA	300 W	361.00	1.40	-/-	[5]
DMCR-1NH	9.1% IPA	300 W	2588.00	10.20	5/79.2%	[6]
$Ni_{4\%}/O_{0.2}$tCN	10% EtOH	300 W	2464.00	14.90	5/81.0%	[7]
CN-COF	10% EtOH	300 W	2623.00	9.80	4/91.0%	[8]
COF-BTT-TAPT	90% EtOH	300 W	620.00	0.46	5/55.3%	[9]
CdS NRs-48h	10% IPA	300 W	2974.70	3.33	4/56.2%	[10]
CoP/Co@NPC-15-g-C_3N_4	10% IPA	300 W	940.00	3.00	3/89.0%	[11]
CC_3N_5-550	10%TeOA	300 W	359.97	12.86	-/-	[12]
P-g-C_3N_4	10% EtOH	300 W	1095.16	/	5/94.0%	[13]
PSI/C_3N_4-2	10% IPA	350 W	1000.78	/	5/92.6%	[14]
SCN2	10% IPA	300 W	416.70	8.6	5/63.3%	[15]
CNT	10% IPA	AM 1.5	2480.00	18	4/83.0%	[16]
Nv-CNN-3	10% EtOH	300 W	1780.00	10.5	4/92.9%	[17]
NDCN	10% IPA	300 W	476.00	8.2	5/98.7%	[18]

UCN4	10% EtOH	300 W	330.36	2..19	3/77.7%	[19]
KCT5-5	10% IPA	500 W	890.56	/	3/96.2%	[20]
OCN-500	10% IPA	300 W	1200	10.2	4/96.9%	[21]
g-C_3N_4	10% EtOH	2 kW	125	11.76	-/-	[22]
50Co/CN	10% EtOH	300 W	3200	/	7/93.5%	[23]
DCNS	10% EtOH	300 W	3080	3.51	4/83.2%	[24]
Cu@Au/$BiVO_4$	5% MeOH	/	625	/	5/87.9%	[25]
Fl-CN-530	10% EtOH	300 W	1893	9	5/89.2%	[26]
KCMCN	0.5%IPA	/	794.8	7.5	5/96.7%	[27]
m-CNNP	10% IPA	/	43.07	0.55	10/71.4%	[28]
C_3N_5-8P-0.9CoPc	10% EtOH	300 W	3080.30	21.02	5/93.2%	This work

Table S3. The Bader charge of the photocatalytic.

			C_3N_5-CoPc		C_3N_5-P-CoPc	
	C_3N_5	CoPc	C_3N_5	CoPc	C_3N_5-P	CoPc
Charge	360	177	360.03	176.97	360.74	176.26

Table S4. The Bader charge of Co atom in different samples.

	CoPc	C_3N_5-CoPc	C_3N_5-P-CoPc	C_3N_5-P-CoPc/OO
Charge	7.94	7.90	7.81	7.69

Reference

[1] Y. Q. Tang, F. S. Ye, B. R. Li, T. Y. Yang, F. Y. Yang, J. F. Qu, X. G. Yang, Y. H. Cai, J. D. Hu, *Small*, 2024, 2400376.

[2] X. Ma, H. F. Cheng, *Chem. Eng. J.*, 2022, **429**, 132373.

[3] L. Shi, L. Q. Yang, W. Zhou, Y. Y. Liu, L. S. Yin, X. Hai, H. Song, J. H. Ye, *Small*, 2018, **14**, 1703142.

[4] Y. Xie, Y. X. Li, Z. H. Huang, J. Y. Zhang, X. F. Jia, X. S. Wang, J. H. Ye, *Appl. Catal. B*, 2019, **265**, 118581.

[5] H.-i. Kim, Y. Choi, S. Hu, W. Y. Choi, J.-H. Kim, *Appl. Catal. B*, 2018, **229**, 121-129.

[6] P. Das, G. Chakraborty, J. Roeser, S. Vogl, J. Rabeah, A., *J. Am. Chem. Soc.*, 2023, **145**, 2975-2984.

[7] R. F. Du, K. Xiao, B. Y. Li, X. Han, C. Q. Zhang, X. Wang, Y. Zuo, P. Guardia, J. S. Li, J. B. Chen, J. Arbiol, A. Cabot, *Chem. Eng. J.*, 2022, **441**, 135999.

[8] D. Xin, X. M. Lv, H. Z. Wang, F. S. Chen, S. Y. Wang, G. F. Zheng, B. Wang, Q. Han, *Chem. Eng. J.*, 2022, **455**, 140124.

[9] M. J. Liu, P. P. He, H. T. Gong, Z. H. Zhao, Y. M. Li, K. Zhou, Y. M. Liu, J. Li, Z. B. Bao, Q. W. Yang, Y. W. Yang, Q. L. Ren, Z. G. Zhang, *Chem. Eng. J.*, 2024, **482**, 148922.

[10] Y. G. Zhang, H. W. Huang, L. C. Wang, X. L. Zhang, Z. J. Zhu, J. J. Wang, W. Y. Yu, Y. H. Zhang, *Chem. Eng. J.*, 2022, **454**, 140420.

[11] Q. J. Ji, L. H. Pan, J. X. Xu, C. Wang, L. Wang, *ACS Appl. Energy Mater.*, 2020, **3**, 3558-3567.

[12] S. F. Ng, J. J. Foo, W. J. Ong, *Mater. Horiz.*, 2024, **11**, 408.

[13] X. K. Xu, Z. H. Zhang, *Catal. Sci. Technol.*, 2024, **14**, 3374.

[14] L. J. Hu, Z. C. Ding, F. Yan, Y. M. Du, Q. X. Xiao, H. Q. Wang, *Appl. Surf. Sci.*, 2023, **638**, 158135.

[15] Y. N. Li, W. Wang, Y. Wang, H. C. He, X. Yu, D. Xia, L. Deng, Y. N. Liu, *Chem. Eng. Sci.*, 2023, **282**, 119333.

[16] J. W. Chen, W. Gao, Y. C. Lu, F. S. Ye, S. W. Huang, Y. Y. Peng, X. G. Yang, Y. H. Cai, J. F. Qu, J. D. Hu, *ACS Appl. Nano Mater.*, 2023, **6**, 3927-3935.

[17] C. Zhao, C. J. Shi, Q. Li, X. Y. Wang, G. Zeng, S. Ye, B. J. Jiang, J. Liu, *Mater Today Energy*, 2021, **24**, 100926.

[18] J. Luo, Y. N. Liu, C. Z. Fan, L. Tang, S. J. Yang, M. L. Liu, M. Wang, C. Y. Feng, X. L. Ouyang, L. L. Wang, L. Xu, J. J. Wang, M. Yan, *ACS Catal.*, 2021, **11**, 11440-11450.

[19] C. Q. Zhou, Y. H. Song, Z. H. Wang, J. Y. Liu, P. P. Sun, Z. Mo, J. J. Yi, L. Z. Zhai, *J. Environ. Chem. Eng.*, 2023, **11**, 110138.

[20] S. Y. Zhou, S. L. Cheng, J. H. Han, New J. Chem. 2023, **47**, 19063.

[21] Z. Wei, M. L. Liu, Z. J. Zhang, W. Q. Yao, H. W. Tan, Y. F. Zhu, *Energy Environ. Sci.*, 2018, **11**, 2581.

[22] Y. Shiraishi, S. Kanazawa, Y. Sugano, D. Tsukamoto, H. Sakamoto, S. Ichikawa, T. Hirai, *ACS Catal.*, 2014, **4**, 774-780.

[23] Y. L. Peng, L. Z. Wang, Y. D. Liu, H. J. Chen, J. Y. Lei, J. L. Zhang, *Eur. J. Inorg. Chem.*, 2017, 4797-4802.

[24] Q. He, B. Viengkeo, X. Zhao, Z. Y. Qin, J. Zhang, X. H. Yu, Y. P. Hu, W. Huang, Y. G. Li, *Nano Res.*, 2021, **16(4)**, 4524-4530.

[25] K. Y. Wang, M. Wang, J. C. Yu, D. Liao, H. Y. Shi, X. F. Wang, H. G. Yu, *ACS Appl. Nano Mater.*, 2021, **4**, 13158-13166.

[26] B. Feng, Y. N. Liu, K. Wan, S. J. Zu, Y. Pei, X. X. Zhang, M. H. Qiao, H. X. Li, B. N. Zong, *Angew. Chem. Int. Ed.*, 2024, **63**, e202401884.

[27] Q. X. Cao, X. L. Wu, Y. X. Zhang, B. Yang, X. F. Ma, J. Song, J. M. Zhang, *J. Catal.*, 2022, **414**, 64-75.

[28] W. Liu, C. J. Song, M. P. Kou, Y. Y. Wang, Y. Deng, T. Shimada, L. Q. Ye, *Chem. Eng. J.*, 2021, **425**, 130615.